Calibration of Pipeline Steel Model for Computational Running Ductile Fracture Assessment

Gaute Gruben[1], Stéphane Dumoulin[1], Håkon Nordhagen[1], Morten Hammer[2] and Svend Tollak Munkejord[2]
[1] Materials and Nanotechnology, SINTEF Industry
Trondheim, Norway
[2] Gas Technology, SINTEF Energy Research
Trondheim, Norway

ABSTRACT

A novel fracture calibration method is presented for material models applied in finite element analysis of pipeline steels exposed to running ductile fracture. The calibration is based on the drop-weight tear test which is commonly applied for qualification of pipeline steels. The method is applied on three L450 steels with low, medium and high impact toughness. The calibrated fracture models are used in a numerical analysis of a full-scale fracture propagation test where the crack-driving force stems from a CO_2-rich mixture that initially is in a dense phase. The results from the simulations are compared with experimental results.

KEY WORDS: Running ductile fracture; finite element analysis; computational fluid dynamics; drop-weight tear test

INTRODUCTION

Running ductile fracture is an event that must be considered in design of a pipeline. The problem was thoroughly studied at the Battelle Memorial Institute during the 1960s and 70s, and this resulted in the semi-empirical two-curve method, see Maxey (1974), which is applied in several codes and recommended practices, e.g. (ISO/TC 265, 2016, DNV-GL, 2017). However, for pipelines made of modern high-strength steels, pipelines transporting rich gases, and in particular pipelines transporting dense liquid-phase carbon dioxide, the two-curve method has proven to be inaccurate and non-conservative (Cosham et al., 2014, Leis, 2015, Biagio et al., 2017, Michal et al., 2018). To address and overcome this problem, numerical methods have been developed, e.g. (O'Donoghue et al., 1991, Shim et al., 2008, Meleddu et al., 2014, Nakai et al., 2016, Botros et al., 2018). Most numerical approaches, however, focus on natural gas and seldomly include backfill. Over the last years, SINTEF has developed a numerical tool that couples a Finite Element (FE) solver which calculates the response of the pipe and the backfill with a Computational Fluid Dynamics (CFD) solver that calculates the fluids decompression and the pressure distribution in the cross-section (Nordhagen et al., 2012, Aursand et al., 2016, Nordhagen et al., 2017). In our model we have chosen to discretize the pipe segments using shell elements with an approximate in-plane size equal to the wall thickness. With such a coarse discretization, it is impossible to capture the complex phenomenon occurring close to the crack-tip of a propagating fracture, such as tunneling and shear banding. However, the element size is sufficient to capture the local necking phenomenon and can give a good estimate of the material behavior at this length scale. To accomplish this, a good calibration routine for the material model, including fracture, is needed. In previous studies a calibration routine based on the Charpy V-notch test and a virtual uniaxial tensile test have been applied to calibrate the fracture criterion (Nordhagen et al., 2017, Gruben et al., 2018), but this approach predicted the crack to propagate faster than what was observed in the experiments for a high toughness steel, see Gruben et al. (2018). In contrast to the Charpy test with a 10x10mm cross section, the drop-weight tear test (DWTT) usually applies the full thickness of a pipe section. Due to the relatively large size of the specimen, the DWTT gives a good indication of the state of the material prior to fracture in a running fracture event in a pipe. In this study we present a hybrid experimental-numerical methodology for calibration of a propagating ductile fracture model for relatively large shell elements based on the DWTT set-up.

EXPERIMENTAL

Data from the full-scale and small-scale experiments presented by Cosham et al. (2016) are employed in this study. The test program included a full-scale fracture propagation test as shown in Fig. 1. Here the pipe sections exposed to running fracture are sketched along with designation pipe number, pipe end marking, pipe section length and Charpy V-notch toughness. As can be seen from Fig. 1 the set-up was telescopic with increasing fracture toughness away from the initiation pipe. The pipe sections were of Grade L450 steel and had a nominal outer diameter of 610 mm and a nominal wall thickness of 19.1 mm. Material test specimens were cut from each end of each pipe section. The material test matrix consisted of uniaxial tensile tests, Charpy V-notch tests and pressed-notched drop-weight tear tests. Table 1 compiles the average values for each pipe section in terms of thickness (t), yield strength (YS), tensile strength (TS), Charpy V-notch energy (CVN) and drop-weight tear test energy (DWTT) at room temperature. The shear area in all drop-weight tear tests was 97%, or larger, of the initial cross-section – indicating ductile behavior of all pipe segments at the test temperature. All the drop-weight tear tests were instrumented and the resulting force-

displacement curves from the tests are shown in Fig. 2 together with results from FE simulations performed in this study.

In the fracture propagation test, the loading stemmed from impure CO_2 with an initial pressure of 151.2 bar and an initial temperature of 15ºC. After depressurization, a two-phase state was reached at approximately 90 bar, while the loading pressure at the crack-tip was estimated as 82–84 bar. This high loading was due to the initial pressure and temperature and the impurities consisting of 1.1 mol-% hydrogen, 6.6 mol-% nitrogen and 2.0 mol-% oxygen.
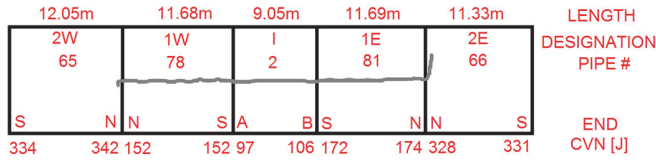

Fig. 1   Sketch of the telescopic set-up and the crack-path. The bottom numbers indicate CVN energies in pipe sections.

Table 1. Average values of thickness (t), yield strength (YS), tensile strength (TS), Charpy V-notch energy (CVN) and drop-weight tear test energy (DWTT) from the pipe sections.

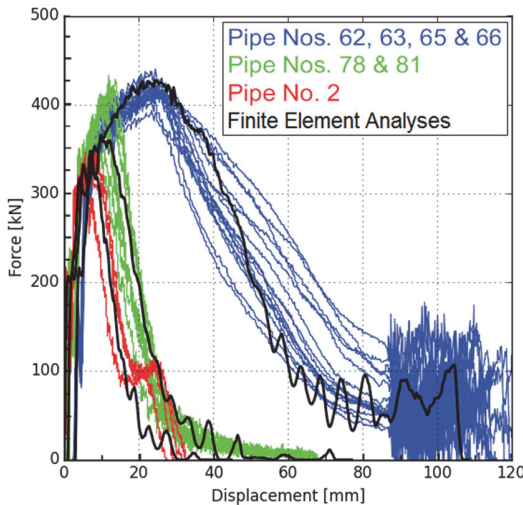| Test	2W	1W	I	1E	2E
t [mm]	19.7	19.1	19.4	19.2	19.5
YS [MPa]	525	475	470	490	530
TS [MPa]	601	589	577	600	609
CVN [J]	343	152	102	173	330
DWTT [J]	24771	6988	4282	7140	20592

Fig. 2   Force-displacement curves from drop-weight tear tests and FE simulations.

CONSTITUTIVE MATERIAL MODEL

The elastic properties of the steel pipe material are described by a Young's modulus of 210 GPa and a Poisson ratio of 0.3. A visco-thermo-plasticity model based on the von Mises yield surface and associated flow rule is applied to describe the plastic flow. The flow stress, σ_f, is defined by an extended Voce hardening rule (Voce, 1948) with multiplicative strain-rate and temperature dependency taken from the modified Johnson-Cook model (Børvik et al., 2001), and is expressed as

$$\sigma_f = \left[\sigma_0 + \sum_{i=1}^{2} Q_i \left(1 - \exp\left(-\frac{\theta_i}{Q_i} p \right) \right) \right] \left(1 - \frac{\dot{p}}{\dot{p}_0} \right)^c \left[1 - \left(\frac{T - T_0}{T_0 - T_m} \right)^m \right] \quad (1)$$

where $\dot{p}$ is the equivalent plastic strain-rate and $p = \int \dot{p} dt$ is the equivalent plastic strain. The initial yield stress is given by σ_0, while Q_i and θ_i are parameters governing the work hardening. The parameters c and $\dot{p}_0$ are controlling the strain rate sensitivity. T is the material temperature, while T_0 is the reference temperature, T_m is the melting temperature and m is an exponent controlling the temperature influence on the flow stress. The Taylor-Quinney coefficient is set to 0.9, i.e. 90% of the plastic work is adiabatically converted to heat, which is a common assumption (Børvik et al., 2001).

By inspecting Eq. 1 it is clear that more data than the yield strength and tensile strength are needed to determine the materials stress-strain curves. The following procedure to estimate the flow stress curves for the three materials was applied by Gruben et al. (2018), but is repeated here for convenience. The procedure is based on the empirical method presented by Liessem et al. (2007) where the work hardening for various pipeline steels is estimated from the yield strength to tensile strength ratio and Hollomon's equation; $\sigma_f = A \cdot p^n$. The parameters A and n are estimated as by the equations proposed by Lu et al. (2015) as

$$n = 0.151 \left(\ln\left(2 - \frac{YS}{TS} \right) \right)^{0.461} + 0.575 \left(\ln\left(2 - \frac{YS}{TS} \right) \right)^{1.61} \quad (2)$$

$$A = TS \left(\frac{e}{n} \right)^n, \ e = 2.71828... \quad (3)$$

When the parameters in Hollomon's equation are established, the Voce hardening curve can be fitted to Hollomon's curve using the least-squares method. As can be seen from Table 1, the pipes in the east and west directions had very similar material properties, thus only the initiation pipe (I) and the first and second test pipes in the east direction (1E and 2E) are calibrated. The Hollomon and Voce parameters are given in Table 2. The materials strain-rate sensitivity is assumed to be similar to the X65 steel investigated by Nordhagen et al., (2012), and so the parameters $c = 0.011$ and $\dot{p}_0 = 0.015 / \text{s}$ are applied. The adiabatic heating of the steels is modelled with a reference temperature $T_0 = 293 \text{ K}$, melting temperature $T_m = 1800 \text{ K}$, and linear temperature sensitivity on the flow stress, i.e. $m = 1$. The applied thermal parameters are in line with modelling assumptions in several other studies on steels, e.g. (Børvik et al., 2001, Børvik et al., 2009).

Table 2. Calibrated material parameters for pipe sections I, 1E and 2E.

	I	1E	2E
A [MPa]	802	833	800
n [-]	0.100	0.099	0.077
σ_0 [MPa]	470	492	531
Q_1 [MPa]	216	223	170
Θ_1 [MPa]	439	455	369
Q_2 [MPa]	139	144	117
Θ_2 [MPa]	3884	4052	3664

FRACTURE MODEL AND CALIBRATION

In our modelling approach of the running fracture problem, we apply shell elements to discretize the pipe sections and the element erosion technique to model the propagating crack. When the fracture criterion is met in an element, the crack propagates one increment equal to the element size in the pipe's longitudinal direction. If small solid elements were applied to model the propagating crack, the simulations would be too computationally expensive, and so shell elements with an initial length in the longitudinal direction equal to the thickness of the pipe wall and an initial length in the hoop direction equal to half the pipe wall thickness have been applied in previous studies (Nordhagen et al., 2017, Gruben et al., 2018). In order to provide the necessary data for the shell element fracture calibration, FE analyses of the pressed-notch DWTT tests were conducted. The pressed-notch DWTT test is a good choice for performing calibration due to the size of the specimen and the crack propagation mode which is close to the crack propagation mode in a pipeline running fracture, but also since this test is widely used in line pipe assessment (Hara et al., 2008, Hara, 2016) which enabels access to test data.

Simulation of DWTT tests

The in-plane geometry of the DWTT FE models followed API RP 5L3 (American Petroleum Institute, 2014), and the thickness is equal to the nominal pipe thickness, i.e. 19.1 mm. Two symmetry planes are applied in the FE models; in the thickness direction and in the longitudinal direction of the specimen. The specimen is supported by a cylinder with a diameter of 38.1 mm, and the striker is modelled as a cylinder with diameter 50.8 mm that impacts the sample at its center with a velocity of 9.0 m/s and an energy of 50 kJ. Both the support and the striker are modelled with a rigid body formulation. The specimen is discretized by hexahedral elements with selectively reduced integration (LS-DYNA type -1), and the characteristic element size in the region where fracture occurred is 0.3 mm. The element size is in the same range as in a detailed DWTT FE model presented by Nonn et al. (2018) . The explicit solver of LS-DYNA (LSTC, 2015) is applied for running the simulations of the DWTT tests. The constitutive relation from Eq. 1 is applied with the given strain-rate sensitivity parameters and the Voce parameters from Table 2. A Coulomb friction coefficient of 0.2 is applied between the specimen and the striker and the specimen and the support. The fracture is modelled by element erosion and the Cockcroft-Latham (CL) fracture model (Cockcroft and Latham, 1968). The CL model can be expressed as a damage variable D that evolves as a function of the major principal stress, σ_I, and the plastic strain as

$$D = \frac{1}{W_C} \int_0^p \max(0, \sigma_I) dp \qquad (4)$$

An element is deleted as the damage variable D equals unity in one integration point.

For each of the three materials, the fracture parameter W_C was adjusted so that the absorbed energy in the simulation was within 5% of the values given in Table 1. The simulations were controlled by comparing the simulated force-displacement curves with the experimental curves as shown in Fig. 2. Due to the good agreement between the simulated and experimental force-displacement curves, it is assumed that the FE models can provide data of sufficient accuracy for calibration of fracture criteria for large shell elements.

Calibration for large shell elements

As previously mentioned, the shell elements intended for use in the full-scale crack propagation test have an initial length equal to the nominal pipe wall thickness (here 19.1 mm), and an initial length in the hoop direction of half the wall thickness (here 9.55 mm). To capture the deformation at this length scale from the DWTT test, the displacement histories from four nodes located at positions corresponding to the shell element size were collected from the solid elements in the DWTT simulation, see Fig. 3(a). The time at onset of fracture is determined as the instant when the crack on the surface of the specimen reaches the y-position of the top nodes as indicated in Fig. 3(b). Since the crack propagates in a tunneling mode, see Fig. 4, the time at onset of fracture relevant for a shell element is deemed to be when the fracture is complete through the thickness, i.e. when it has reached surface of the specimen as in Fig. 4 (b). The nodal displacement histories were then applied as loading on one singe shell element up to the time at onset of fracture, enabling calibration of the fracture criterion for the shell element. Here a shell element with reduced integration is applied, i.e. one in-plane integration point at the center of the element plane is present. Since the shell element is exposed to pure membrane loading, the integration points through the thickness are exposed to the same stress and strain histories. Any fracture criteria applicable for shell elements in combination with the element erosion technique can be calibrated based on the displacement histories from the DWTT simulations. Here, two fracture criteria have been calibrated for each of the three materials, the CL criterion as defined by Eq. 4, and the maximal principal strain criterion (MPS). The latter determines onset of fracture when the principal strain ε_I reaches a critical value, ε_I^C. The shell element deformation in the DWTT test has a principal strain direction along the x-direction as defined in Fig. 3(a), thus the MPS criterion applies as a Mode I criterion. Since ε_I is defined by the x-displacement, it can be considered as a large-scale CMOD criterion. It is noted that the CL criterion considers both the deformation in the x and y direction.
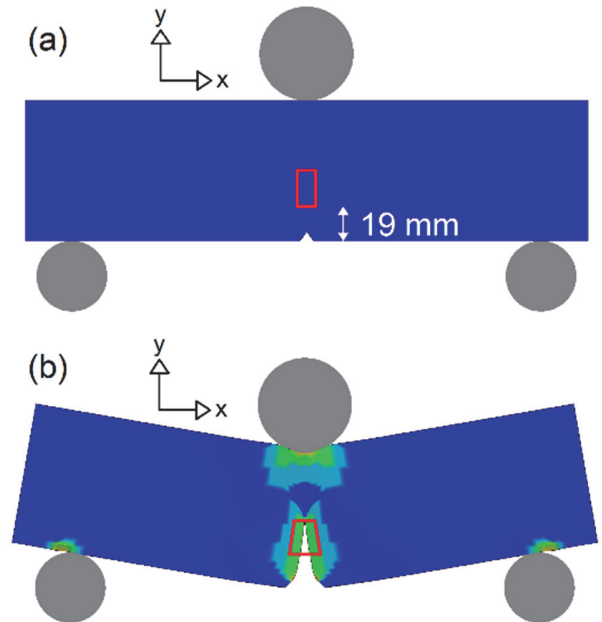

Fig. 3 Results from pipe segment 1E. The contours are equivalent plastic strain. (a) The corners of the red square indicate the initial position of the nodes applied for shell-element fracture calibration. (b) The red trapezoid indicates the nodal positions for the shell element calibration at determined onset of fracture.

Table 3. Calibrated fracture parameters for pipe sections I, 1E and 2E. The CL criterion is calibrated for small solid elements (W_C^{solid}) and large shell elements (W_C^{shell}).

	I	1E	2E
W_C^{solid} [MPa]	320	475	1120
W_C^{shell} [MPa]	247	350	728
ε_I^C [-]	0.255	0.355	0.715

The position of the lowermost nodes for calibrating the shell element fracture criterion is 19 mm above the bottom of the specimen as shown in Fig. 3(a). With a notch depth of 5.1 mm, this gives 13.9 mm crack propagation before the lowermost nodes for shell element calibration is reached, and so any effects connected to fracture initiation are not influencing the shell calibration. On the other hand, the uppermost nodes for shell element calibration are positioned close to the neutral bending axis of the DWTT specimen and can be exposed to compression in the initial deformation. Another calibration having a height of 10 mm between the bottom nodes and the bottom of the specimen was also conducted, and this calibration gave results within 2% of those given in Table 3. Thus, it is assumed that consistent results from the shell element calibration will be achieved as long as the position of the nodes used for calibration are on the tension side of the DWTT bending axis and allow for some propagation before entering the lowermost nodes.
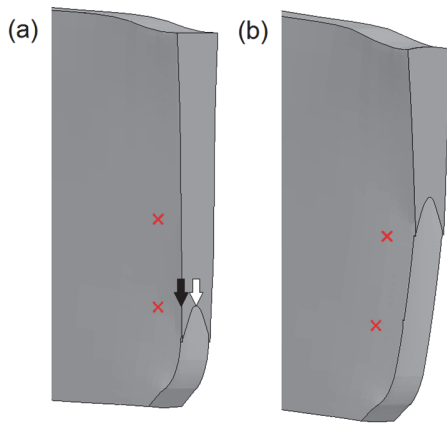

Fig. 4   FE simulation of the 1E DWTT test. Configuration of DWTT specimen as (a) fracture enters the height of the lower node applied for shell element fracture calibration and (b) as the crack leaves height of the upper node applied for shell element calibration. The red crosses indicate the nodes used for shell element fracture calibration and the arrows indicate the positions of the solid elements that are applied in collecting time histories.

Stress-state, strain rate and temperature

The mechanical state of the material at the center of the DWTT specimen differs from the state at the surface. Also, the length scale over which the state is evaluated influences the results. To illustrate the differences, the histories of the equivalent plastic strain, the stress triaxiality, the equivalent plastic strain rate and the temperature were collected from solid elements located at the center and at the surface of the specimen shown by respectively the white arrow and the black arrow in Fig. 4(a). In addition, the same histories were collected from the shell element applied in the calibration process. The data was collected for all three steel materials, and the results are compiled in Fig. 5.

The stress triaxiality is defined as the ratio of the mean stress to the von Mises equivalent stress. High values of stress triaxiality indicate that the material is under high tensile loading, which promotes growth of microvoids and therefore a more rapid ductile fracture. As expected, Fig. 5 shows that the stress triaxiality is higher in the solid elements at the center of the DWTT specimen than in the solid elements at the surface. Since the CL fracture criterion predicts lower ductility for higher stress triaxiality, the equivalent plastic strain at fracture is lower at the center of the DWTT specimen than at the surface. The surface solid element has a stress triaxiality which is very similar to the shell element for all three materials. This is due to the plane stress condition which is present on the surface of the specimen. As can be expected, the equivalent plastic strain at fracture is largest for the 2E material, and the 1E material displays a larger fracture strain than the I material. Notably all three materials display a kink in the stress triaxiality at a plastic strain equal to approximately half the fracture strain. A similar behavior has been observed in other studies, (Nonn and Kalwa, 2013, Nonn et al., 2018). The reason for the decrease in triaxiality may be due to blunting of the crack tip and development of a free surface on the element prior to element deletion.

The equivalent strain at fracture in the shell and solid elements are of the same order, but the strain rate in the solid elements reaches values about 20-25 times the strain rates in the shell element, as shown in Fig. 5. The shell element is approximately 50 times larger than the solid element, and the amount of time for the crack to propagate through the shell element is much larger than in the solid element, giving a significantly lower strain rate. It is noted that onset of fracture in the center element occurs after ~1.0 ms in the I material, while it occurs in the 1E and 2E materials at ~1.5 ms and ~3.0 ms, respectively. The time at onset of fracture reflects the speed of the propagating crack which is lower for increased ductility. The speed of the propagating crack also influences the strain rate, which for the I material is nearly twice the strain rate in the 2E material. As can be seen in Fig. 5 the center element is deleted prior to the surface element, while the shell element is deleted later. The difference in time at onset of fracture in the two solid elements is due to the tunneling mode as shown in Fig. 4(a), while the shell element is deleted later as shown in Fig. 4(b).

The temperature increases proportionally with the plastic work. Thus, the 2E material has a significantly larger increase in temperature than the other two materials. Furthermore, the surface solid elements reach higher temperatures than the center solid elements and the shell elements. Similarly to the strain rate histories, the length scale of the shell elements gives a significantly smaller rate of the temperature increase than what is seen in the solid elements. As seen in Fig. 5, the temperature increase in 2E is ~200°C, while the temperature increase in 1E and I are ~75°C and ~50°C, respectively. Additional FE simulations of the DWTT tests were run to investigate the effect of neglecting softening due to adiabatic heating. It was found that the effect on the I and 1E materials is insignificant, while for the 2E material the peak force level was reduced by ~4% and the absorbed energy was reduced by ~2%. Thus, the effect of including softening due to adiabatic heating is small on the global level. On the local level, the solid elements had a somewhat smaller strain and larger stress at fracture when excluding the effect of adiabatic softening. Calibrating the CL fracture criterion for a shell element, without taking into account adiabatic heating provides very similar values for W_C^{shell}. The MPS criterion on the other hand, was calibrated with a fracture strain 6% lower when neglecting adiabatic heating for the 2E material. Again, the effect on the I and 1E materials were neglectable. In conclusion, the effect of including adiabatic heating in the calibration process can be important for a high-toughness material if a strain-based fracture criterion is applied, but not including adiabatic heating will provide a conservative estimate.
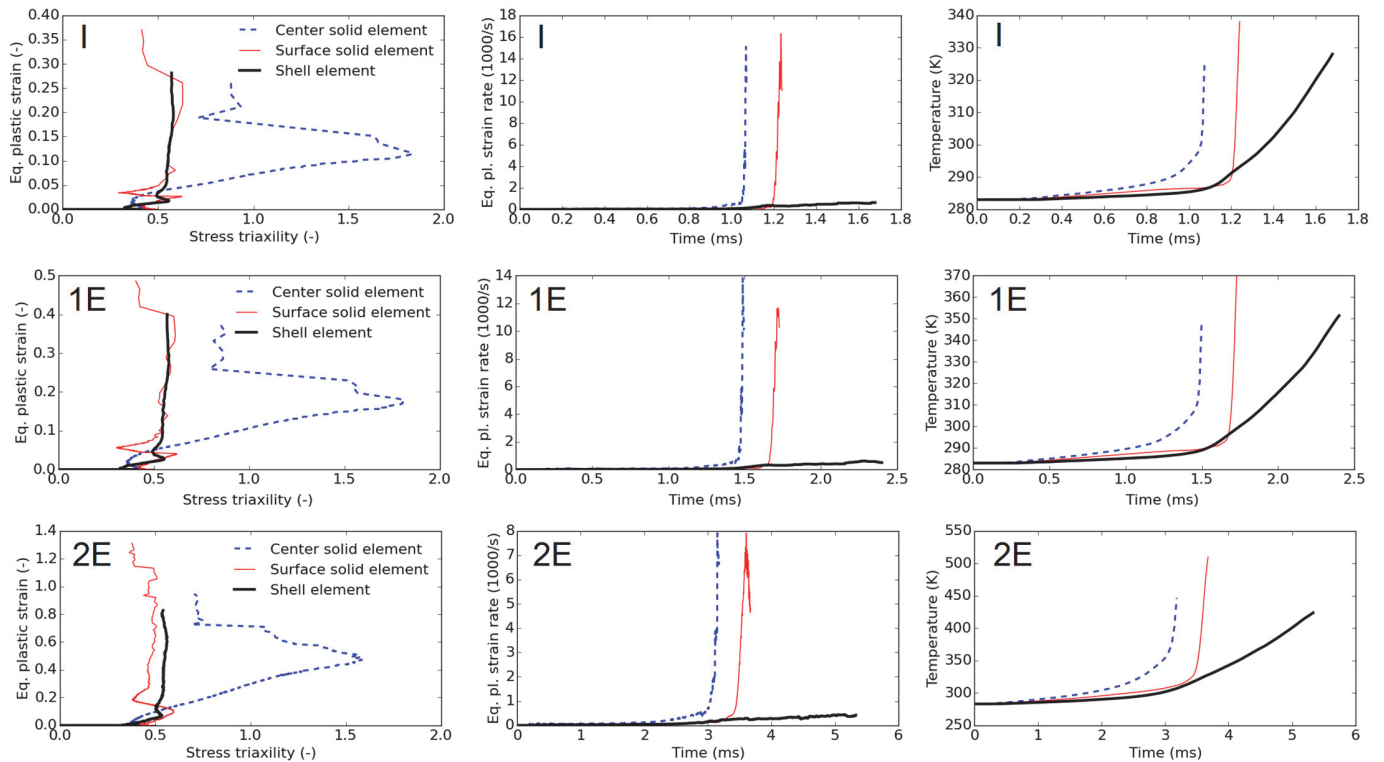
Fig. 5 Equivalent plastic strain as function of stress triaxiality and time histories of the strain rate and the temperature for each material. The values are collected from the center solid element and the surface solid element in the DWTT FEA and from the shell element applied for calibration.

ASSESSMENT ON A FULL-SCALE BURST TEST

A numerical model of a full-scale crack propagation test was presented by Gruben et al. (2018). The same model is applied here, but now with the above presented fracture models calibrated from the drop-weight tear tests. The simulations are run with the SINTEF coupled FE-CFD code. Here the pipe sections constitute the structure which is exposed to loading from the escaping CO_2 fluid, and boundary conditions from the surrounding soil. Fig. 6 shows the initial geometry of the pipe segments and the surrounding soil. The pipe is discretized by shell elements, while the backfill is discretized by SPH particles and an Eulerian mesh is applied to describe the decompression of the fluid. A full coupling between the fluid and structure is applied in the simulations. More details can be found in (Gruben et al., 2018).
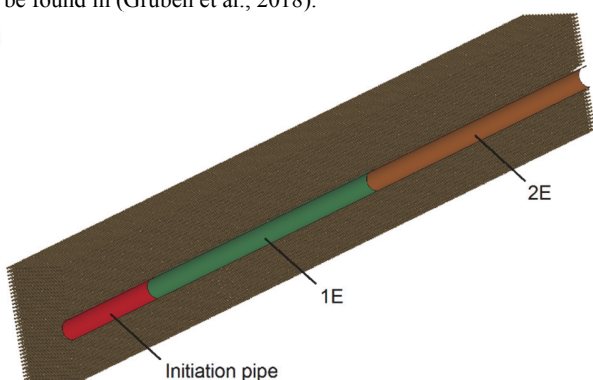

Fig. 6 Geometry of the three sections and the surrounding soil in the full-scale model. Half the model is blanked out for visualization.

The results from the coupled FE-CFD model in terms of crack velocity as function of crack position is shown in Fig. 7. For the initiation section, both CL and MPS criterion simulations overestimate the crack velocity. The simulation with the CL criterion also overestimates the crack velocity in the medium toughness 1E section, while the MPS criterion simulation provides a good estimate of the crack velocity. In the experiment, the crack propagated a short distance into the sections 2E and 2W before arrest occurred. A somewhat longer crack is present in the simulation with both fracture criteria, and especially for the simulation with the CL criterion. In (Gruben et al., 2018), the CL criterion was applied in the FE-CFD simulation, but here a different calibration procedure was applied. The resulting resistance to fracture was predicted well in the low and medium toughness sections, but too little resistance was predicted in the high-toughness section. With the calibration based on the DWTT test, both CL and MPS criterion provide a more consistent result, i.e. consistently underpredicting the resistance to crack propagation within the whole toughness range, and so providing more conservative results. Based on this observation, the DWTT based calibration is deemed more robust than the previous calibration method based on the Charpy V-notch and a virtual tensile test.

Four additional calibrations and FE-CFD simulations were run for each of the two fracture criteria. Here, the element size was perturbed by a factor 1.5 in the longitudinal direction and in the hoop direction. A significant size effect was observed when perturbating the element size in both the longitudinal and the hoop direction. This result suggests that the stress-state as measured on the shell element length scale in the DWTT and the full-scale test are not entirely similar. By inspecting the deformed elements at onset of fracture in the DWTT and the full-scale simulations, it is observed that the shell element in the DWTT FEA is

exposed to compression in the crack direction, while the shell element in the full-scale test undergoes tension in the crack direction before onset of fracture. To illustrate this, the 1st principal strain (which points in the transverse/hoop direction) is plotted as a function of the 2nd principal strain (which points in the crack propagation direction) in Fig. 8. Another aspect is that while the DWTT shell element is exposed to pure membrane deformation, the full-scale shell element also has a small bending component. Hillerborg et al. (1976) suggested a regularization scheme to compensate for differences in element size. Here a softening function applies to the element from the moment a fracture criterion is met, and the energy absorbed after onset of fracture is depending on the element size. Since the fracture in the DWTT test is propagating in a tunneling mode, onset of fracture for the shell element in the calibration could be defined as the instant when the crack reaches the lower nodes as shown in Fig. 4 (a). A linear decay of element strength could then be assumed until the shell element is fully fractured as shown in Fig. 4 (b). Another possible approach to remedy the length scale effect, at least in the hoop direction, is to apply cohesive elements in combination with a calibrated cohesive energy, or the node release algorithm used by O'Donoghue et al. (1997) in combination with the a critical CTOA value.
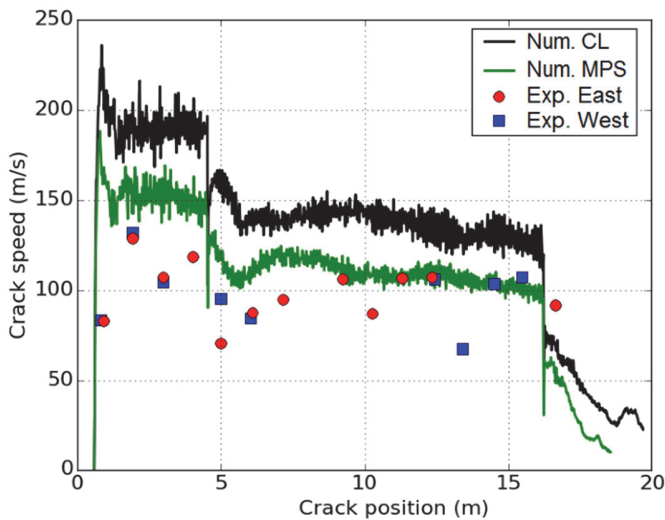

Fig. 7   Crack-speed as function of crack position in west and east direction in the experiment and in the numerical simulations with the CL and the MPS fracture criteria.
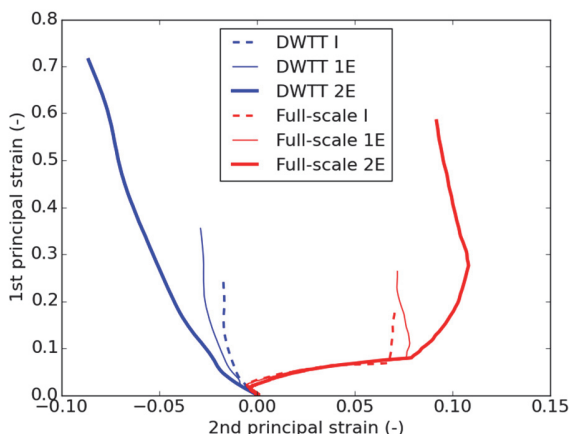

Fig. 8   Histories of first and second principal strains till onset of fracture from shell elements used in calibration (DWTT) and shell elements used in full-scale simulations with CL criterion.

CONCLUSIONS

Three pipeline materials considered as low-toughness, medium-toughness and high-toughness steels, have been calibrated to two different fracture criteria for FE simulation crack propagation with large shell elements. The calibration procedure is based on the pressed-notched DWTT set-up, and a hybrid experimental-numerical approach is applied to extract the data used for calibration. The calibrated criteria are applied in simulations of a full-scale crack-propagation test, and both fracture criteria provide consistent and conservative results with respect to the toughness of the steel sections. Some mesh sensitivity is present in the analysis, and further research is needed to address this.

ACKNOWLEDGEMENTS

REFERENCES

American Petroleum Institute (2014). "Recommended Practice for Conducting Drop-Weight Tear Tests on Line Pipe, Fourth Edition."

Aursand, E, Dumoulin, S, Hammer, M, Lange, HI, Morin, A, Munkejord, ST & Nordhagen, HO (2016). "Fracture propagation control in CO2 pipelines: Validation of a coupled fluid–structure model." *Engineering Structures,* 123**,** 192-212.

Biagio, MD, Lucci, A, Mecozzi, E & Spinelli, CM (2017). "Fracture Propagation Prevention on CO2 Pipelines: Full Scale Experimental Testing and Verification Approach." *Pipeline Technology Conference.* Berlin.

Botros, KK, Clavelle, EJ, Uddin, M, Wilkowski, G & Guan, C (2018). "Next Generation Ductile Fracture Arrest Analyses for High Energy Pipelines Based on Detail Coupling of CFD and FEA Approach." *ASME Paper No. IPC2018-78097.*

Børvik, T, Dey, S & Clausen, AH (2009). "Perforation resistance of five different high-strength steel plates subjected to small-arms projectiles." *International Journal of Impact Engineering,* 36**,** 948-964.

Børvik, T, Hopperstad, OS, Berstad, T & Langseth, M (2001). "A computational model of viscoplasticity and ductile damage for impact and penetration." *European Journal of Mechanics - A/Solids,* 20**,** 685-712.

Cockcroft, MG & Latham, DJ (1968). "Ductility and the workability of metals." *J. Inst. Metals,* 96**,** 33-39.

Cosham, A, Jones, DG, Armstrong, K, Allason, D & Barnett, J (2014). "Analysis of two dense phase carbon dioxide full-scale fracture propagation tests." *ASME Paper No. IPC2014-33080.*

Cosham, A, Jones, DG, Armstrong, K, Allason, D & Barnett, J (2016). "Analysis of a Dense Phase Carbon Dioxide Full-Scale Fracture Propagation Test in 24 Inch Diameter Pipe." *ASME Paper No. IPC2016-64456.*

DNV-GL (2017). "DNVGL-RP-F104 Design and operation of CO2 pipelines."

Gruben, G, Dumoulin, S, Nordhagen, H, Hammer, M & Munkejord, ST (2018). "Simulation of a Full-Scale CO2 Fracture Propagation Test." *ASME Paper No. IPC2018-78631.*

Hara, T (2016). "Mechanism of Arrowhead Fracture Occurrence in

DWTT." *Proc 6th Int Ocean and Polar Eng Conf,* Rhodes, Greece. ISOPE-I-16-223.

Hara, T, Shinohara, Y, Terada, Y & Asahi, H (2008). "DWTT Properties For High Strength Line Pipe Steels." *Proc 18th Int Offshore and Polar Eng Conf.* Vancouver, Canada. ISOPE-I-08-242.

Hillerborg, A, Modéer, M & Petersson, PE (1976). "Analysis of crack formation and crack growth in concrete by means of fracture mechanics and finite elements." *Cement and Concrete Research,* 6**,** 773-781.

ISO/TC 265 (2016). "ISO 27913:2016   Carbon dioxide capture, transportation and geological storage -Pipeline transportation systems."

Leis, B (2015). "Arresting propagating shear in pipelines." *Steel in Translation,* 45**,** 1.

Liessem, A, Knauf, G & Zimmermann, S (2007). "Strain Based Design—What the Contribution of a Pipe Manufacturer Can Be." *roc 17th Int Offshore and Polar Eng Conference*, Lisbon, Portugal. ISOPE-I-07-500.

LSTC (2015). "LS-DYNA KEYWORD USER'S MANUAL." *LS-DYNA R8.0 03/23/15 (r:6319).* Livermore, California 94551-0712: Livermore Software Technology Corporation.

Lu, C, Michal, G & Venton, P (2015). "A new fracture velocity model for high grade gas pipelines." *20th Joint Technical Meeting on Pipeline Research.* Paris.

Maxey, WA (1974). "Fracture Initiation, Propagation and Arrest." *5th Symposium on Line Pipe Research.* Huston, Texas.

Meleddu, A, Bertoli, M, Di Biagio, M & Demofonti, G (2014). "CO2 Decompression Modeling for Ductile Fracture Propagation Control in Deepwater Pipelines." *Proc 24th Int Ocean and Polar Eng Conf.* Busan, Korea. ISOPE-I-14-602.

Michal, G, Davis, B, Østby, E, Lu, C & Røneid, S (2018). "CO2SAFE-ARREST: A Full-Scale Burst Test Research Program for Carbon Dioxide Pipelines — Part 2: Is the BTCM Out of Touch With Dense-Phase CO2?." *ASME Paper No. IPC2018-78525*.

Nakai, H, Shibanuma, K & Aihara, S (2016). "Numerical model for unstable ductile crack propagation and arrest in pipelines using finite difference method." *Engineering Fracture Mechanics,* 162**,** 179-192.

Nonn, A & Kalwa, C (2013). "Analysis of dynamic ductile fracture propagation in pipeline steels: A damage mechanics approach." *Proceedings of the 6th International Pipeline Technology Conference.* Ostend.

Nonn, A, Paredes, M, Keim, V & Wierzbicki, T (2018). "Comparison of Fracture Models to Quantify the Effects of Material Plasticity on the Ductile Fracture Propagation in Pipelines." *ASME Paper No. IPC2018-78366*.

Nordhagen, HO, Kragset, S, Berstad, T, Morin, A, Dørum, C & Munkejord, ST (2012). "A new coupled fluid–structure modeling methodology for running ductile fracture." *Computers & Structures,* 94-95**,** 13-21.

Nordhagen, HO, Munkejord, ST, Hammer, M, Gruben, G, Fourmeau, M & Dumoulin, S (2017). "A fracture-propagation-control model for pipelines transporting CO2-rich mixtures including a new method for material-model calibration." *Engineering Structures,* 143**,** 245-260.

O'Donoghue, PE, Green, ST, Kanninen, MF & Bowles, PK (1991). "The development of a fluid/structure interaction model for flawed fluid containment boundaries with applications to gas transmission and distribution piping." *Computers and Structures,* 38**,** 501-513.

O'Donoghue, PE, Kanninen, MF, Leung, CP, Demofonti, G & Venzi, S (1997). "The development and validation of a dynamic fracture propagation model for gas transmission pipelines." *International Journal of Pressure Vessels and Piping,* 70**,** 11-25.

Shim, D-J, Wilkowski, G, Rudland, D, Rothwell, B & Merritt, J (2008). "Numerical Simulation of Dynamic Ductile Fracture Propagation Using Cohesive Zone Modeling." *ASME Paper No. IPC2008-64049*.

Voce, E (1948). "The Relationship between Stress and Strain for Homogeneous Deformation." *Journal of the Institute of Metals,* 74**,** 537-562.